



Contents lists available at ScienceDirect

International Journal of Rock Mechanics & Mining Sciences

journal homepage: www.elsevier.com/locate/ijrmms

Mechanical behavior and permeability evolution of gas infiltrated coals during protective layer mining

Guangzhi Yin^{a,b,c}, Minghui Li^{a,b,c,*}, J.G. Wang^d, Jiang Xu^{a,b,c}, Wenpu Li^{a,b,c}^a State Key Laboratory of Coal Mine Disaster Dynamics and Control, Chongqing University, Chongqing 400030, China^b State and Local Joint Engineering Laboratory of Methane Drainage in Complex Coal Gas Seam, Chongqing University, Chongqing 400030, China^c College of Resource and Environmental Sciences, Chongqing University, Chongqing 400030, China^d School of Mechanics and Civil Engineering, China University of Mining and Technology, Xuzhou 221116, China

ARTICLE INFO

Article history:

Received 27 February 2015

Received in revised form

21 August 2015

Accepted 24 August 2015

Available online 10 November 2015

Keywords:

Protective layer mining

Effective stress

Gas pressure

Stress–strain relation

Permeability

ABSTRACT

This study investigated the stress–strain–permeability relationship of a Chongqing coal under the stress path during the mining process. The abutment stress was first measured at the longwall (LW) face 3211 of Songzao Mine in Chongqing, China. The field monitoring results revealed that the concentration coefficient of the abutment stress was approximately 1.5–2.0 during protective layer mining. Then, triaxial compression tests for the gas-infiltrated coals were conducted under the above stress path and different gas pressures. These tests, with the simultaneous actions of unloading confining stress and loading axial stress, are called SUL tests. The triaxial compression tests revealed that the peak deviatoric stress and the corresponding strain of coal under SUL tests were lower than those under conventional triaxial compression (CTC) tests. Poisson's ratio was higher, but the elastic modulus was lower in SUL tests. The permeability evolution of coal under the SUL tests underwent four distinct stages: the increasing stage in the process of SUL, decreasing stage, slowly increasing stage beyond the yield point, and sharply increasing stage after the peak stress. With the increased gas pressure, the peak deviatoric stress and corresponding axial strain decreased, Poisson's ratio increased, and elastic modulus decreased. Further, the permeability of coal increased with increasing gas pressure in the complete deformation process.

© 2015 Elsevier Ltd. All rights reserved.

1. Introduction

Coal mining induces different stress zones in front of the working face of coal—a relief stress zone, abutment stress zone, and recovered stress zone—from the initial in-situ stress state.¹ During this coal mining process, the stress path experiences the loading of axial stress and the simultaneous unloading of confining stress. However, current investigations on the coupling mechanism between the mechanical behavior and permeability of coal are almost all based on conventional triaxial compression (CTC) tests. This CTC path may not represent the coal mining process. It is necessary to validate the applicability of the current investigations to the coal mining process.

The stress evolution of coal seams has been widely investigated. A series of three-dimensional numerical models were developed to examine the effect of the mining depth, in-situ stress and stope geometry as well as the orientation on the overbreak of a stope wall.² For example, Wang et al. took the cutting face from

disaster sites as prototypes to study the effect of the stress distribution on dynamic disasters of coal mines.³ Guo et al. presented a comprehensive study on the longwall in a deep underground coal mine.⁴ They investigated the mining-induced strata movement, stress changes, fracture openings, and gas flows. Their studies included the field monitoring of overburden displacement, changes of stress and water pressure at the LW face. They concluded that the vertical stress increased and the horizontal stress decreased during mining. All of the above investigations revealed that deeper mining faces a higher risk of mining disasters.

Coal seam gas couples with coal deformation to affect mining safety. In China, coal seams are rich in coal seam gas. There is approximately 10 billion m³ of the recoverable coalbed methane (CBM) in China. The Erlian basin in Inner Mongolia contains 2 billion m³ of recoverable CBM. The Ordos basin and Qinshui basin contain more than 1 billion m³ of recoverable CBM. The gas content gradually increases with coal burial depth. The accumulation of coal seam gas during mining may trigger dynamic disasters, such as gas emission, and even the occurrence of coal and gas outburst in front of the working face. The gas accumulation depends on many parameters, of which the permeability evolution of coal is the most important. Therefore, the investigation of the

* Corresponding author.

E-mail address: cqumhli@foxmail.com (M. Li).

permeability distribution within coal and the surrounding rocks is the core work of the simultaneous extraction of coal and gas.

Stress-dependent permeability has been investigated for different rocks and coals.^{5–7} An exponential function was proposed to describe the relationship between coal permeability and stress.^{8,9} Coal is a type of organic porous rock with a strong sorption capacity for coal seam gas. This desorption of the gas may induce the volumetric shrinkage of coal matrix¹⁰ and change the coal permeability.¹¹ For example, Meng and Li investigated the permeability of high-rank coals during early depletion of CBM and found that the permeability of high-rank coals was susceptible to effective stress.¹² Therefore, the mechanical behavior and permeability evolution should be the focus.

The mechanical behavior and permeability evolution have been investigated in recent years.^{13,14} For example, Chen et al. studied the damage process of reconstituted coal specimens and its influence on permeability during an unloading process.¹⁵ They combined X-ray CT scanning and permeability experiments to measure the mechanical behavior and permeability evolution of reconstituted coal specimens subjected to the same stress path and the same effective confining stress. Cai et al. explored the contribution of interactions between stress and damage on the evolution of permeability through X-ray computed tomography images and acoustic emission profiling together with concurrent measurements of the P-wave velocity.¹⁶ Zhang et al. investigated the experimental relationships among the flowrate, permeability and fracture aperture in fractured media.¹⁷ Qiu et al. designed an incrementally cyclic loading-unloading pressure test to quantify stress-induced microfracturing and fracturing under the condition of confining stress reduction.¹⁸ On the other hand, Wang et al. experimentally investigated the role of gas desorption, stress level and loading rate on the mechanical behavior of methane infiltrated coal.^{19,20} The deformation, strength and permeability evolution were studied through the conventional triaxial compression of initially intact coal. Zhao et al. studied the influence of gas adsorption on the permeability evolution of fractured porous media under 3D stress conditions.²¹ The relationships among effective stress, gas desorption, matrix shrinkage, gas slippage, and permeability were explored.^{22–27} The above experimental studies were all based on CTC tests. Before the application of the above results to different mining processes, it is necessary to identify the difference of the mechanical behavior and permeability evolution of coal under the CTC tests and the simultaneous action of the unloading confining stress and loading axial stress (SUL) tests.

This study investigated the mechanical behavior and permeability evolution of gas infiltrated coals during protective layer mining. This paper is composed of three parts. First, the change of the abutment stress in front of the working face was monitored at LW face 3211 of Songzao Mine in Chongqing, China. This field monitoring obtained the concentration coefficients of the abutment stress. A stress path with the loading rate of axial stress and the unloading rate of confining stress was thus determined for the triaxial compression tests. Second, a coupling experiment on the mining-induced mechanical behavior and permeability evolution of coal under the SUL path was conducted in a complete deformation process, from elastic deformation to failure. The coupling mechanism between the mining-induced mechanical behavior and permeability of coal was explored. Finally, the implication of the above experimental results to the safety assessment for underground protective layer mining was discussed.

2. Measurement of in-situ abutment stress during protective layer mining

This section will present the field measurement for the change

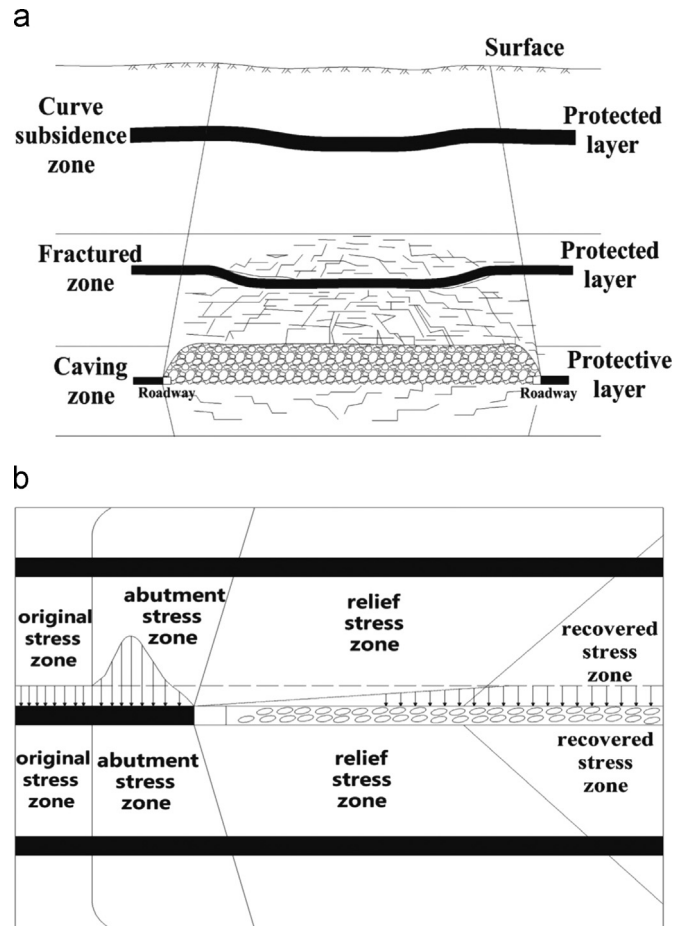


Fig. 1. Schematic diagram and stress distribution of the protective layer mining. (a) Schematic diagram of the protective layer mining. (b) Stress zones of coal and rock seams along the strike direction.

of in-situ stress during the mining process. These results can provide a stress path for the laboratory tests for the measurement of the mechanical behavior and permeability evolution of coal.

2.1. Stress zones of coal and rock seams along the strike direction

Protective layer mining is one of the most effective mining methods for gas control in China.^{28,29} This method is schematically drawn in Fig. 1(a). It divides the coal seam into protective layers and protected layers. The protective layers are mined first for the reduction of the gas content in adjacent layers. The protected layers are protected by mining the protective layers. The stress in the protected layers is released by mining the protective layers such that the fractures in the protected layers are open and the permeability is enhanced. As shown in Fig. 1(b), the layers along the strike direction can be divided into four stress zones: the original stress zone, abutment stress zone, relief stress zone, and recovered stress zone. Protective layer mining disturbs the protected layers and breaks the in-situ stress balance. This disturbance causes the coal seams to deform and even to be damaged. The peak abutment stress in the protected layers is obviously decreased. Therefore, different mining methods may have their stress paths and cause different mechanical behavior and permeability evolution of coal seams.

2.2. Field monitoring of stress at LW face 3211

LW face 3211 is the first mined working face at the third depth

Table 1
Simplified geological profiles in panel 3211.

Layer number	Lithology	Thickness (m)
1	Alluvium	460
2	Sandstone	5.45
3	Sandy mudstone	2.65
4	Coal seam	1.83
5	Sandy mudstone	7.43
6	Limestone	1.25
7	Sandstone	3.96
8	Limestone	1.01
9	Sandy mudstone	3.18
10	Argillaceous limestone	4.90
11	Coal seam	0.75
12	Sandy mudstone	3.72
13	Coal seam	0.24
14	Sandy mudstone	3.41
15	Siliceous limestone	1.56
16	Calcareous mudstone	1.19

level of Songzao Mine. Table 1 lists the geological profile of this LW face. This profile was drawn based on a typical borehole log. This LW face is located in a protected layer called coal seam K₂b. The overburden depth ranges between 500 m and 540 m with a 460–500 m thick alluvium layer at the top. The LW face is 1100 m long and 130 m wide. It has a dip angle ranging from 35° to 37° and an average thickness of 0.75 m, ranging from 0.22 m to 1.20 m. The coal seam K₂b is a gas infiltrated layer, with a gas content of 10.14 m³/t. The temperature in the coal seam K₂b is in the range of 28.5 °C to 29.3 °C. The retreat LW mining method with full seam extraction was used, and a “U”-type ventilation system was installed at the LW face for gas ventilation.

2.2.1. Monitoring system design

To understand the mining-induced stress change, a real-time monitoring system, as shown in Fig. 2, was designed based on the specific mining and geological conditions at LW face 3211. Fifteen monitoring stations were installed at a retreat distance of 10–80 m from the LW start-up, with a distance of 5 m each in both the transportation roadway and the ventilation roadway. At each station, one borehole stress meter was installed at a depth of 7 m into the roof of the coal seam to measure the mining-induced stress change. The locations of these borehole stress meters are shown in Fig. 2(a) for the plane view and Fig. 2(b) for the section view.

The measurement of the borehole stress meter is based on the following principle. The initial frequency f_{i0} and the sensor constants B and C of the borehole stress meter were measured after its installation. At different excavation distances of LW face 3211, the frequency values of the borehole stress meter were measured in the same direction. The stress in that direction was then calculated by

$$\sigma_i = C(f_i^2 - f_{i0}^2) - B(f_i - f_{i0}) \tag{1}$$

where B and C are sensor constants, f_{i0} and f_i are the initial frequency and current frequency in that direction, and σ_i is the stress in that direction.

2.2.2. Abutment stress at LW face 3211

The abutment stresses at LW face 3211 were monitored during the mining process. The measured stresses are presented in Fig. 3 along the distance ahead of the LW face. The first roof weighting came at the time when the LW face was excavated 25 m from the start-up. Fig. 3 shows that the change of the stress experienced a low-high-low process with the distance ahead of the LW face. The longwall can be divided into three stress zones: relief stress zone, abutment stress zone, and recovered stress zone. The relief stress

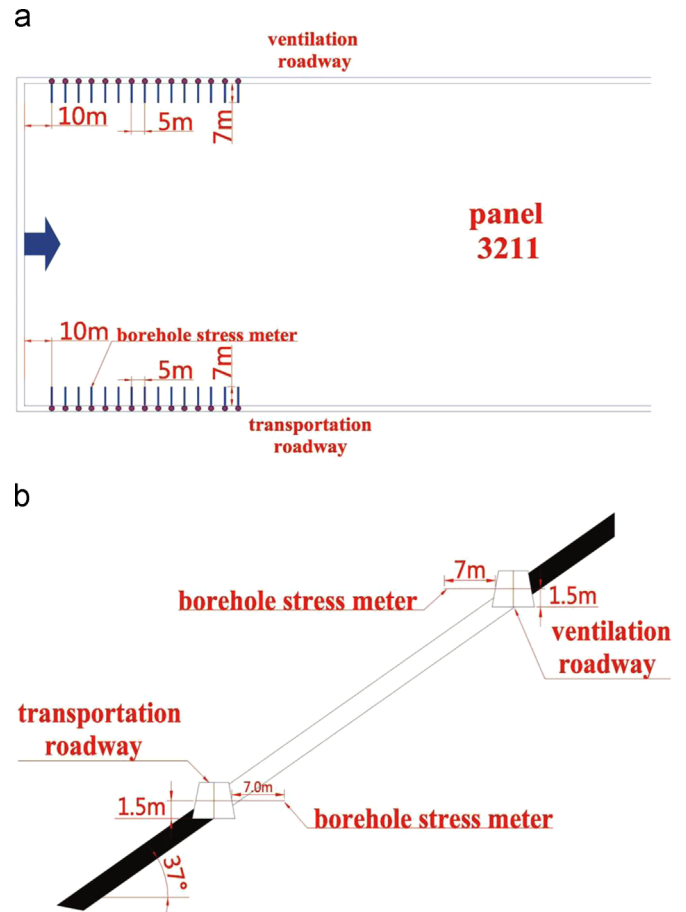


Fig. 2. Location of the borehole stress meters. (a) Plan view. (b) Section view.

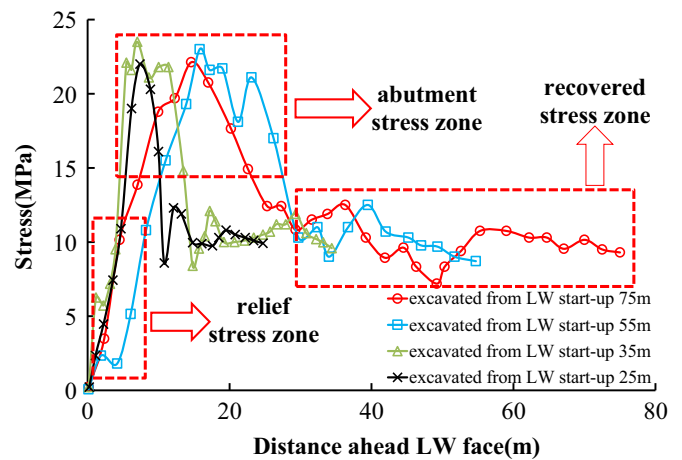


Fig. 3. Measured stress with different distances ahead of the longwall face.

zone refers to the mining-induced stress-relaxed area in the coal and rock seam. The abutment stress zone refers to the area with stress concentration near the LW face. The recovered stress zone refers to the area ahead of the LW face, which is not affected by further mining. The monitoring results showed that the abutment stress reached its peak at the point 18 m ahead of the LW face. After that, the stress gradually decreased and achieved a stable value. These measured stresses indicated that the concentration coefficient of the abutment stress was approximately 1.5–2.0 compared to the in-situ stress state. Further, the horizontal confining stress continuously decreased with the advance of the working face. This field test did not directly measure the change of

this horizontal confining stress, but similar field monitoring showed that this stress was reduced to 0.2–0.6 times its in-situ value.^{1,4} Therefore, the evolution of field stress can be drawn as the following: The in-situ stress state will change with the advance of the working face along a SUL path. This SUL path unloads its confining stress down to 0.2–0.6 times the in-situ stress level and simultaneously loads its axial stress up to 1.5–2.0 times the in-situ stress level. The next section will investigate the mechanical behavior and permeability evolution of coal along this SUL path through laboratory tests.

3. Experiment setup for triaxial compression tests

3.1. Experiment apparatus

The experiment was conducted by using a self-made “THM coupled with triaxial servo-controlled seepage apparatus for gas infiltrated coal”.³⁰ The apparatus is composed of the following main components: a servo loading system, pressure chamber, constant temperature oil heating system, gas pressure control system, data acquisition and storage system, and auxiliary system. This apparatus has the following technical specifications: a maximum axial force of 1000 kN, maximum confining stress of 60 MPa, maximum gas pressure of 20 MPa, maximum axial displacement of 60 mm, and maximum radial deformation of 12 mm. An oil tank is used to adjust the experiment temperature from room temperature to 110 °C. The accuracy of this measurement system is $\pm 1\%$ for stress, $\pm 1\%$ for deformation, and ± 0.1 °C for temperature control.

The following are specially designed to improve the accuracy of both loading and measurement. An installation guide device is equipped to accurately align the pressurized piston rod with the supporting shaft and avoid shaking during the loading process. This helps the specimen be fixed stably and compressed evenly. The servo hydraulic pressure controller performs continuous loading/unloading paths. To let gas pass through the specimen uniformly, a high-permeable pad with multiholes is designed. Such a design makes the experimental conditions quite close to the actual situation of the coal seam gas flow. The constant temperature oil heating system makes the heating process even. The stress, strain, temperature, and gas flow rate are automatically measured by those robust sensors. The loading system is continuously controlled by a computer. This apparatus has system rigidity greater than 10 GN/m and is thus suitable for displacement control. Therefore, this apparatus is applicable to investigate the combined effect of stress, strain, temperature and gas flow on the mechanical behavior and permeability evolution of coal specimens.

3.2. Specimen preparation and testing parameters

Large intact coal blocks were collected and treated from the coal seam according to the “general requirements for sampling (China National Code of GB/T 23561.1-2009)”. The coal blocks were shaped into cylindrical specimens of $\Phi 50 \times 100$ mm. The specimens determined to be without visible fractures and cracks by means of photo observation and statistical classification were

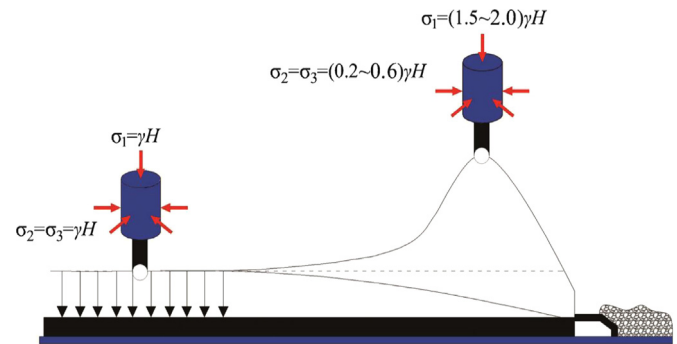


Fig. 4. Mining-induced stress change in protective layer mining.

chosen as the experimental samples. Table 2 lists the main characteristic parameters of the collected coal.

The experimental parameters were carefully selected based on the in-situ mining conditions observed at LW face 3211. In-situ coal and rock were in a hydrostatic pressure state under deep ground stress conditions. The abutment stress increases and the horizontal stress decreased simultaneously along with the removal of working face, which was the real mining-induced stress environment of coal and rock. The mining-induced change of stress during protective layer mining is shown in Fig. 4.

Before mining, the in-situ stress of coal was

$$\sigma_1 = \sigma_2 = \sigma_3 = \gamma H \quad (2)$$

After mining, the stress became

$$\begin{aligned} \sigma_1 &= \alpha \gamma H \\ \sigma_3 &= \beta \gamma H \end{aligned} \quad (3)$$

where γ is the average density of the roof rock (kN/m^3), H is the mining depth (m), α is the concentration coefficient of the abutment stress, and β is the coefficient of horizontal stress. Based on the field monitoring, this study took $\alpha = 1.5$ and $\beta = 0.2 - 0.6$.

3.3. Experiment procedure and data treatment

The axial stress and confining stress in the experiments correspond to the abutment stress and horizontal stress in the field, respectively. The axial stress increases while the confining stress decreases to simulate the changes of the abutment stress and horizontal stress in the field. The experiments strictly followed the following test procedure. Silicon rubber was evenly coated on the coal specimen to prevent gas leakage from the coal. The specimen was installed between the top and bottom pressure shafts in the triaxial chamber after the silicone rubber was fully dry. A thermal shrunken pipe (with an approximately 1 MPa elastic modulus) was then put on. This pipe was heated by a hair dryer so that it closely contacted the specimen wall and both ends of the pressure shafts. The thermal shrunken pipe was then tightened by metal hoops at both ends of the pressure shafts. A circumferential extensometer and the remaining parts of the triaxial flow apparatus were then installed. Three stress paths were used in this laboratory study and are illustrated in Fig. 5. They are described below.

Stress path 1—CTC tests: first, an isotropic in-situ stress state of $\sigma_{10} = \sigma_{30} = 7$ MPa was applied to the specimen. Then, the high-

Table 2
Main characteristic parameters of coal

BET surface area (m^2/g)	Langmuir surface area (m^2/g)	Total pore volume (cm^3/g)	Average pore width (\AA)	Mad (%)	Aad (%)	Vad (%)	FCad (%)
0.2997	0.4744	0.001382	189.5302	1.17	13.16	21.03	64.64

Mad – moisture content on air dried basis; Aad – ash content on air dried basis; Vad – volatile content on air dried basis; FCad – fixed carbon content on air dried basis.

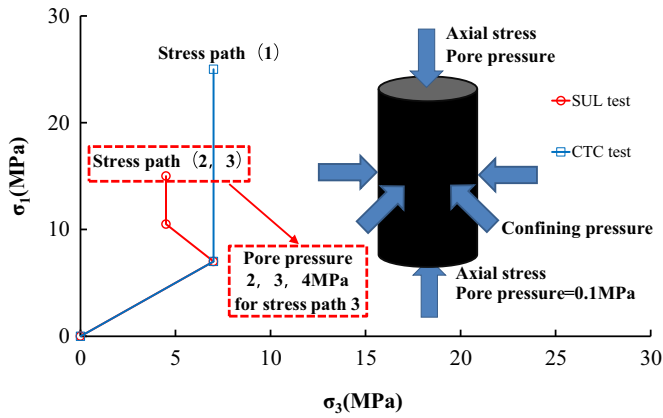


Fig. 5. Stress paths in the experiments.

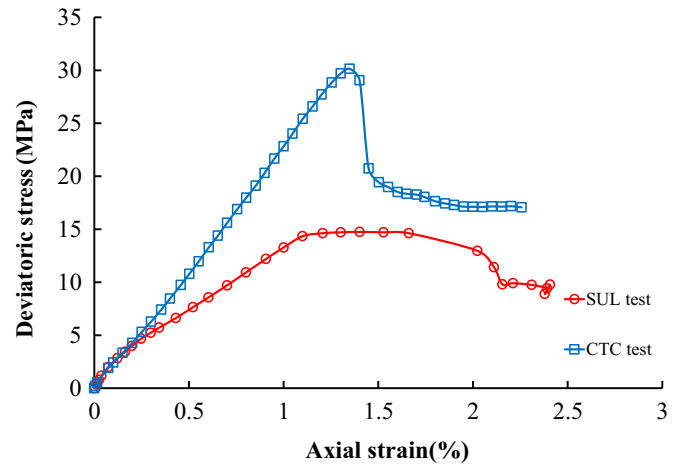


Fig. 6. Deviatoric stress–axial strain curves of coal in the two stress paths.

pressure methane tank was connected to the specimen to inject the methane into the specimen up to the specified gas pressure. The gas outlet valve was closed to maintain constant gas pressure. This state was kept for 12 h to let the coal fully adsorb the methane under this pressure. If the gas pressure did not decrease over the next 2 h, the coal was regarded to be fully saturated by the gas. The gas outlet valve was then opened and maintained at a differential gas pressure of 4 MPa at the two ends of the coal specimen. Finally, axial stress was continuously loaded until reaching peak stress. After reaching the peak stress, the axial stress control was changed to displacement control at a speed of 0.1 mm/min. The experiment was completed when the coal stress was the only residual stress.

Stress path 2—SUL (simultaneous action of unloading the confining stress and loading the axial stress) tests: the isotropic stress and the gas pressure were the same as the above stress path 1. When the axial stress started to be loaded, the confining stress started to be unloaded to 4.5 MPa at a rate of 0.01 MPa/s. This maintained the confining stress higher than the gas pressure throughout the experimental process and ensured that the silicon rubber did not break. The axial stress was continuously applied with a loading rate to ensure that it reached $1.5\sigma_1$ when the confining stress reached 4.5 MPa. The axial stress was continuously loaded, while the confining stress was kept at 4.5 MPa. The axial stress control was changed to displacement control at a speed of 0.1 mm/min after reaching peak stress. The experiment was completed when the coal stress was the only residual stress.

Stress path 3—gas pressure change tests: the stress path was the same as stress path 2, except for the gas pressure. In this stress path, the gas pressure was 2 MPa, 3 MPa and 4 MPa.

The gas permeation through the specimen was assumed to be isothermal, and methane was ideal gas. Thus, the permeability of coal was continuously calculated by^{9,26,31}

$$K = \frac{2q\mu LP_2}{A(P_1^2 - P_2^2)} \quad (4)$$

where K is the permeability (m^2), q is the gas permeation rate (m^3/s), μ is the gas kinematic viscosity (Pa s), L is the length of the coal specimens (m), A is the cross-sectional area of the coal specimens (m^2), P_1 is the gas pressure at the upper stream or inlet of specimens (Pa), and P_2 is the gas pressure at the downstream or outlet of the specimens (Pa).

4. Experimental results and analysis

4.1. Effect of the SUL path on the mechanical behavior

The effect of the SUL path on the mechanical behavior was first

observed by comparing the mechanical behavior under stress paths 1 and 2 (CTC and SUL tests). Fig. 6 presents their deviatoric stress–axial strain curves. Gas pressure causes a volumetric increase (including effective stress effect and adsorption swelling) in the coal. The gas pressure induced volumetric strain was -0.25% for the CTC specimen and -0.24% for the SUL specimen. The CTC test had a much higher peak strength than the SUL test. Their peak strength was 30.14 MPa for the CTC test and 14.75 MPa for the SUL test. The peak strength was reduced by 51.06%. Further, the residual strength for the SUL test was 47% lower than that of the CTC test. They also had different axial strains (defined positive for compression) at peak strength. This strain was 1.21% for the SUL test and 1.35% for the CTC test, a reduction of 10.37%. The CTC test had a higher elastic modulus than the SUL test. These two curves are almost identical at the initial compaction deformation stage because the same initial hydrostatic pressure was applied. The only difference may be due to the heterogeneity of the specimens. The deviatoric stress under the SUL tests increased rapidly because of the unloading of the confining stress. The deformation process after the initial compaction deformation stage was divided into three stages: the first stage was the elastic deformation stage, in which a linear relationship between stress and strain was observed. The second stage was the yield deformation stage, which started from the yield stress point and ended at the peak stress point. In this stage, fractures were generated and evolved up to the specimen failure. Distinct dilatation was observed in this stage. The change rates of the axial strain and radial strain increased rapidly. The last stage was the failure and residual stress stage. In this stage, cracks developed rapidly and crossed each other to form macroscopic fractures. Fig. 7 presents the relationship between the mean stress and the volumetric strain along these two stress paths. Their mean stresses were identical at the initial point. In the SUL test, the mean stress had a slight decrease and then increased slowly up to a maximum volumetric strain. In the CTC test, the mean stress always increased. Further increase of the mean stress caused the coal to dilate quickly. It is noted that the maximum volumetric strain is much larger for the CTC test than for the SUL test. Such behavior is due to the reduction of confining stress in the SUL test.

Their difference were also observed from the Mohr's stress circles in Fig. 8(a) and the stress paths in Fig. 8(b). As observed in the figure, the confining stress of coal was unloaded in the SUL test. This unloading shifted the Mohr's stress circle closer to the failure envelope. The axial stresses were all loaded to the same value, whereas the Mohr's circle of coal under the CTC test was below the failure envelope. Under the SUL test, the Mohr's circle of

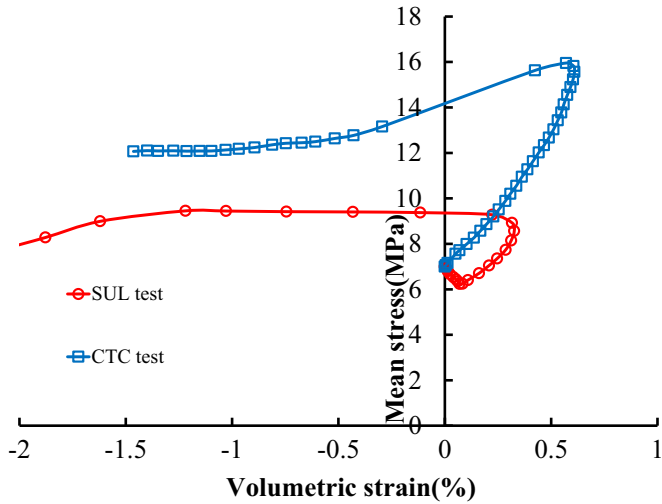


Fig. 7. Mean stress–volumetric strain curves of coal in the two stress paths.

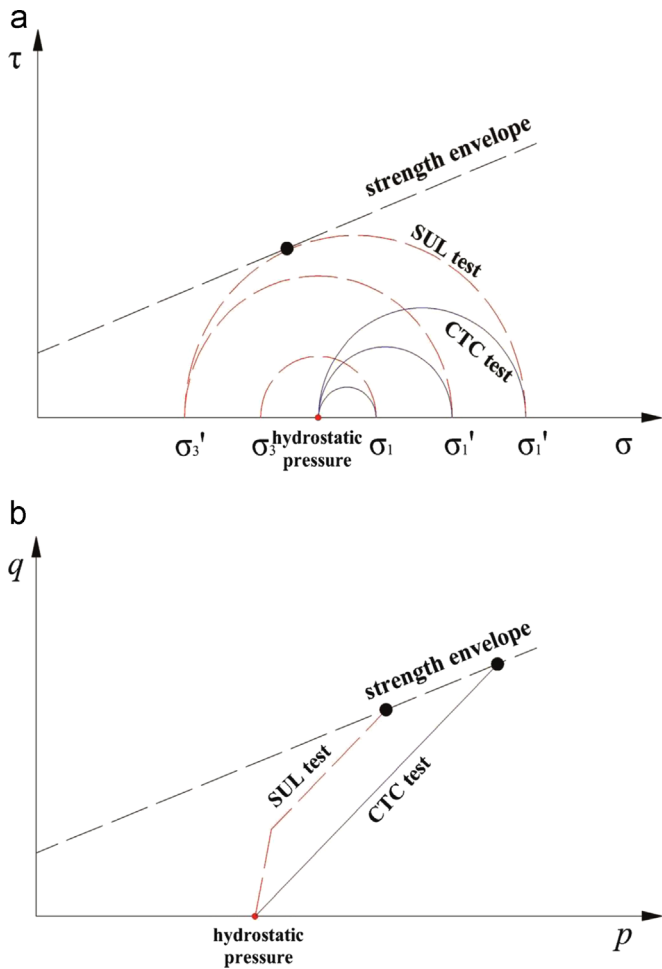


Fig. 8. Stress paths in the two stress paths. (a) Mohr's circles of coal in the two stress paths (stress state comparison with the same σ_1). (b) Stress paths of the experiments along with the failure envelope on a p–q plan.

coal became larger and approached the failure envelope. Therefore, the unloading of confining stress would lead to the failure of coal.

4.2. Effect of the SUL path on permeability evolution

Permeability evolution along the two stress paths was

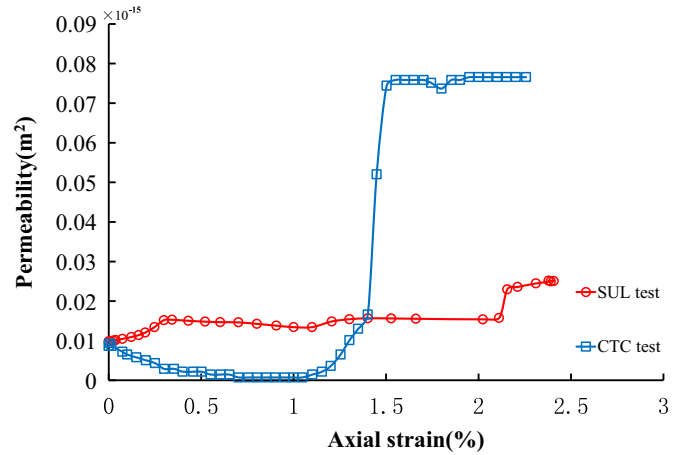


Fig. 9. Relationship between permeability and axial strain in the two stress paths.

observed. Fig. 9 presents their permeability–axial strain curves. At the initial hydrostatic pressure state, the permeability was $0.0098 \times 10^{-15} \text{ m}^2$ for the SUL test and $0.0087 \times 10^{-15} \text{ m}^2$ for the CTC test. This implied that the two specimens had almost the same initial state. However, the permeability evolution depended on the stress path. For the CTC test, the permeability decreased and reached a minimum value around the yield point. Beyond the yield point, the permeability increased quickly. These changes were directly related to the deviatoric stress–strain behavior and deformation stages. This evolution was significantly altered by the following two factors: (1) coal was compacted by the increase of axial stress. The original pores and fractures of coal were compressed. This compaction narrowed the gas flow channels and reduced the permeability of coal. (2) New fractures were generated and evolved with further increases of axial stress. This provided new channels for the gas flow and thus enhanced the permeability of coal. The volumetric strain of coal increased in the initial compaction deformation and elastic deformation stages. In this stage, the original pores and fractures were mainly compressed, and the volume of coal was reduced. This caused the reduction of permeability before the yield point. Beyond the yield point, the original pores and fractures were continuously compressed but not very quickly. At the same time, new fractures were generated and grew faster. In the post-failure stage, the internal structure of coal was damaged, and the fractures expanded, intersected and connected to form macroscopic fractures. The dilatation rate increased such that the permeability of coal increased sharply.

The permeability evolution of coal under the SUL tests was obviously different from that under the CTC tests. This evolution in the whole deformation process can be divided into four stages: the increasing stage in the process of SUL, decreasing stage, slowly increasing stage beyond the yield point, and sharply increasing stage after the peak stress. The relationship between permeability and volumetric or radial strain is explored. Before the dilatation of coal, Fig. 10(a) presents the permeability–volumetric strain curves, and Fig. 10(b) presents the permeability–radial strain curves under these two stress paths. The relationship between permeability and strain under the SUL tests was different from that under the CTC tests, although the initial permeability was almost identical. In the SUL process, the permeability increased to $0.0153 \times 10^{-15} \text{ m}^2$ (increase of 56%), and no decreasing stage was observed. The permeability of coal increased with the volumetric strain in the SUL process (defined as positive for compression), and the specimen was compressed in the process. Fig. 10(b) has a similar pattern. This implies that the radial strain was the key variable to affect the change of permeability in these tests. The stress path has

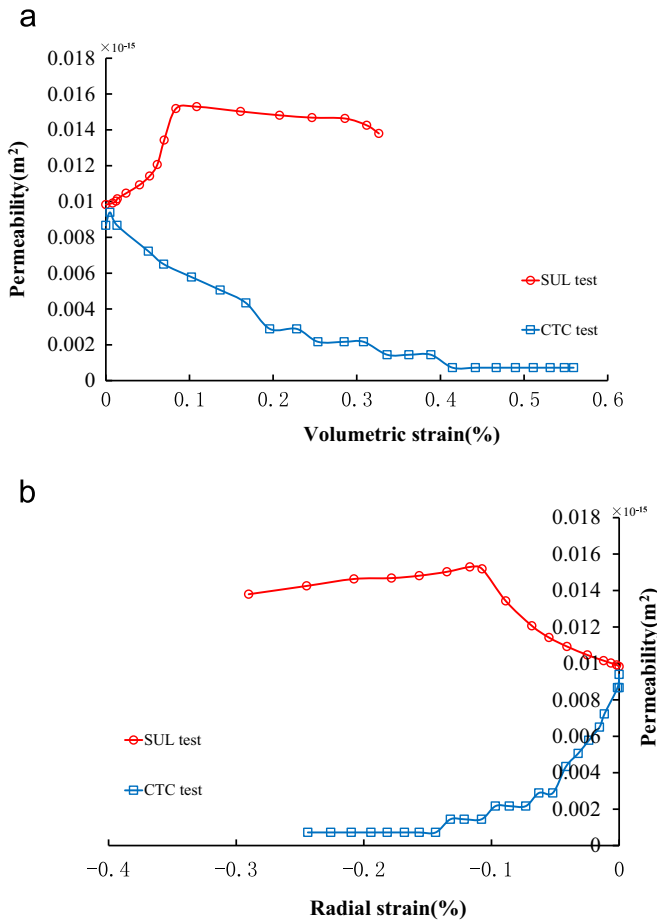


Fig. 10. Permeability–strain curves before the dilatation of coal. (a) Permeability–volumetric strain curves before the dilatation of coal. (b) Permeability–radial strain curves before the dilatation of coal.

significant impacts on the permeability evolution of the coal specimens.

The mechanism for this permeability evolution was explored. In our tests, the flow direction was from the upper end to the lower end of the specimen, thus the gas flow mainly occurred along the vertical fractures. On the other hand, the vertical fractures were more sensitive to confining stress. The unloading of confining stress can untighten the pores, voids and fractures along the vertical direction and enhance the permeability. Therefore, the unloading effect of the confining stress on permeability cannot be ignored in the physical simulation. The axial stress continued to load after the confining stress reached the specified value. This continued the compaction of those pores and fractures already generated thus far and constrained the generation of new fractures. This caused the permeability to decrease slowly. Again, the minimum permeability of $0.0132 \times 10^{-15} \text{ m}^2$ was observed around the yield point of coal. Beyond this point, the coal began to dilate, and its permeability increased slowly. The permeability of coal increased sharply after its peak stress, and new fractures were generated quickly. Therefore, unloading of the confining stress can untighten the pores, voids and fractures, thus enhancing the permeability.

4.3. Effect of gas pressure on the mechanical behavior

As opposed to the above tests, which were conducted under a fixed gas pressure, this section investigated the combined effect of SUL and gas pressure on the mechanical behavior and permeability evolution of coal through different gas pressures. Fig. 11

(a) presents the deviatoric stress–axial strain curves when the gas pressure was 4 MPa, 3 MPa, and 2 MPa. These test results yielded the following behavior. First, the peak strength was higher for the lower gas pressure. The peak deviatoric stress was 14.75 MPa, 31.59 MPa and 39.92 MPa when the gas pressure was 4 MPa, 3 MPa, and 2 MPa, respectively. Further, the corresponding axial strain at the peak deviatoric stress was 1.21%, 2.07% and 2.32%, respectively. Obviously, the peak strength and the corresponding axial strain all decreased with increasing gas pressure. This behavior was induced by two factors. The effective confining stress was reduced with the increase of gas pressure. The decreasing extent of the confining stress caused by the increase of gas pressure was greater than that of the axial stress such that the peak deviatoric stress of coal decreased. Further, the higher gas pressure caused more gas to be adsorbed, which induced the swelling of coal. The gas pressure induced volumetric strain (including the effective stress effect and adsorption swelling) was -0.15% , -0.21% and -0.24% for 2 MPa, 3 MPa and 4 MPa, respectively. The peak deviatoric stress of coal was decreased as the internal swelling stress increased under three-dimensional stress constraints.

The stress–strain relationship was observed under different gas pressures. Fig. 11(b) presents the relationship between deviatoric stress and radial strain. Fig. 11(c) presents the deviatoric stress–volumetric strain curves. Fig. 11(b) reveals that the radial strain of coal decreased with axial loading. The negative strain that implied the dilatation of coal occurred in the radial direction. In the elastic deformation stage, the change rate of the radial strain was smaller than that in the stage of SUL. The radial strain decreased faster with increasing gas pressure. Fig. 11(c) reveals that the volumetric strain of coal increased slowly in the initial stage because of the unloading of the confining stress. The radial strain decreased faster in this stage, which reduced the overall amount of coal compression. The volumetric strain, at the point at which the coal began to dilate, increased as the gas pressure increased, which indicated that the maximum amount of compression increased as the gas pressure increased. Fig. 11(d) presents the relationship between the second invariant of the deviatoric stress tensors and the second invariant of the deviatoric strain tensors of coal for the SUL stress paths under different gas pressures. This is the stress–strain relationship in the general space. This figure reveals that the peak values of the generalized shear stress and the corresponding values of the generalized shear strain all decreased with increasing gas pressure.

Poisson's ratio (ν) is defined as the ratio of radial strain to axial strain in the elastic deformation stage of the uniaxial compression test:

$$\nu = -\frac{d\varepsilon_3}{d\varepsilon_1} \quad (5)$$

where ε_3 is the radial strain, ε_1 is the axial strain, and d denotes the differential increment. This ratio may be not the exact Poisson's ratio in triaxial compression tests. It can be still used to express the loose extent of coal.

The elastic modulus was calculated by the generalized Hooke's law in the elastic deformation stage:

$$E = [\sigma_1 - \nu(\sigma_2 + \sigma_3)]/\varepsilon_1 \quad (6)$$

In any deformation stage, the deformation modulus E_c was calculated as

$$E_c = \frac{1}{d\varepsilon_1} [d\sigma_1 - \nu(d\sigma_2 + d\sigma_3)] \quad (7)$$

The effect of gas pressure on Poisson's ratio and the elastic modulus is presented in Fig. 12. Poisson's ratio increased, but the elastic modulus gradually decreased with increasing gas pressure. This was because more gas was adsorbed at a higher gas pressure.

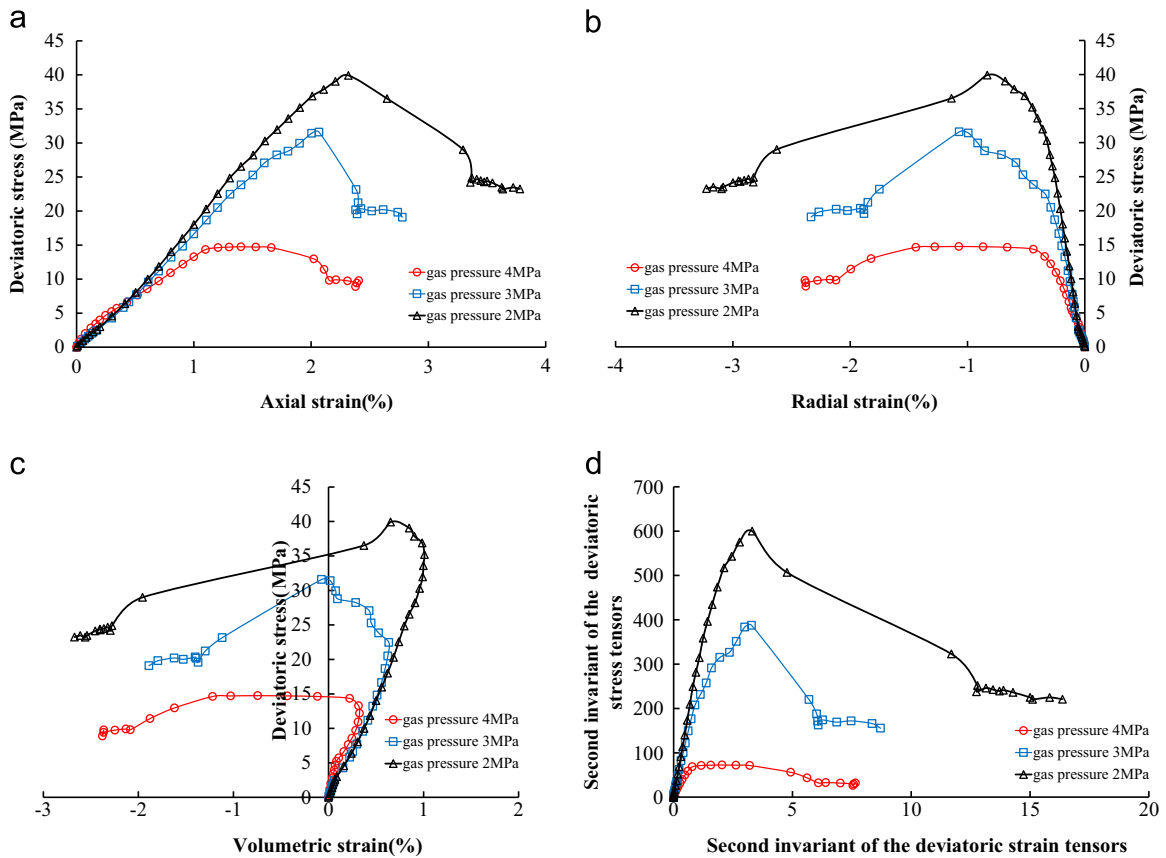


Fig. 11. Effect of gas pressure on stress–strain curves of coal under the SUL path. (a) Effect of gas pressure on deviatoric stress–axial strain curves of coal under the SUL path. (b) Effect of gas pressure on deviatoric stress–radial strain curves of coal under the SUL path. (c) Effect of gas pressure on deviatoric stress–volumetric strain curves of coal under the SUL path and (d) Effect of gas pressure on the second invariants of the deviatoric stress tensors–the second invariants of the deviatoric strain tensors curves of coal under the SUL path.

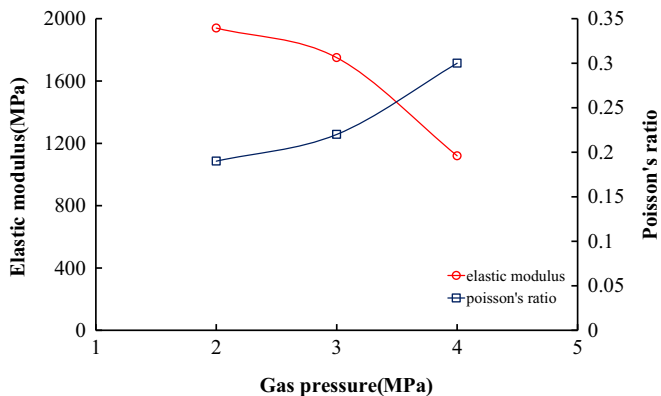


Fig. 12. Change of elastic modulus and Poisson's ratio with gas pressure.

That is, more gas molecules were attached to the surfaces of coal particles, causing more swelling of the coal matrix. On the other hand, a higher gas pressure means a lower effective confining stress and less constraint along the horizontal direction, which promoted the development of original fractures and caused the coal to become looser. Therefore, higher gas pressure in the SUL tests implied less constraint in the horizontal direction and more swelling in the coal matrix. The coal became looser.

Fig. 13(a) presents the change in the ratio of the radial strain to the axial strain with confining stress under different gas pressures. This figure shows that the ratio increased with increasing gas pressure. The three curves have good consistencies under different gas pressures. It is inferred that the ratio increased with the unloading of

confining stress. Fig. 13(b) is the relationship between the deformation modulus and confining stress under different gas pressures. The deformation modulus decreased as gas pressure increased, which means that the deformation modulus decreased with the unloading of confining stress. This was because the radial constraint was weakened in the process of SUL, and the coal became looser.

4.4. Effect of gas pressure on permeability evolution

The permeability evolution was heavily affected by gas pressure. The permeability–axial strain curves are presented in Fig. 14. This figure shows that the permeability evolution can be divided into four stages: the increasing stage in the process of SUL, decreasing stage, slowly increasing stage beyond the yield point, and sharply increasing stage after the peak stress. The permeability increased with the increase of gas pressure in the complete deformation process. Such behavior can be caused by two factors. First, the effective stress of coal decreased with the increase of gas pressure. This expanded the flow channels of coal and increased the permeability of coal. Second, the higher gas pressure caused more gas to be adsorbed on the particle surface of the matrix and led to higher swelling of the coal matrix. This matrix swelling may make the flow channel narrower and reduce the permeability of coal. Therefore, the permeability evolution of coal was the result of these two competitive factors. The Langmuir isotherm shows that adsorbed gas increased rapidly with increasing gas pressure when the gas pressure was low, thus the coal matrix swelled fast at this stage. This led to decreased permeability. When the gas pressure was low, the matrix-swelling factor played the dominant role in the permeability evolution. The increased rate of adsorbed gas decreased

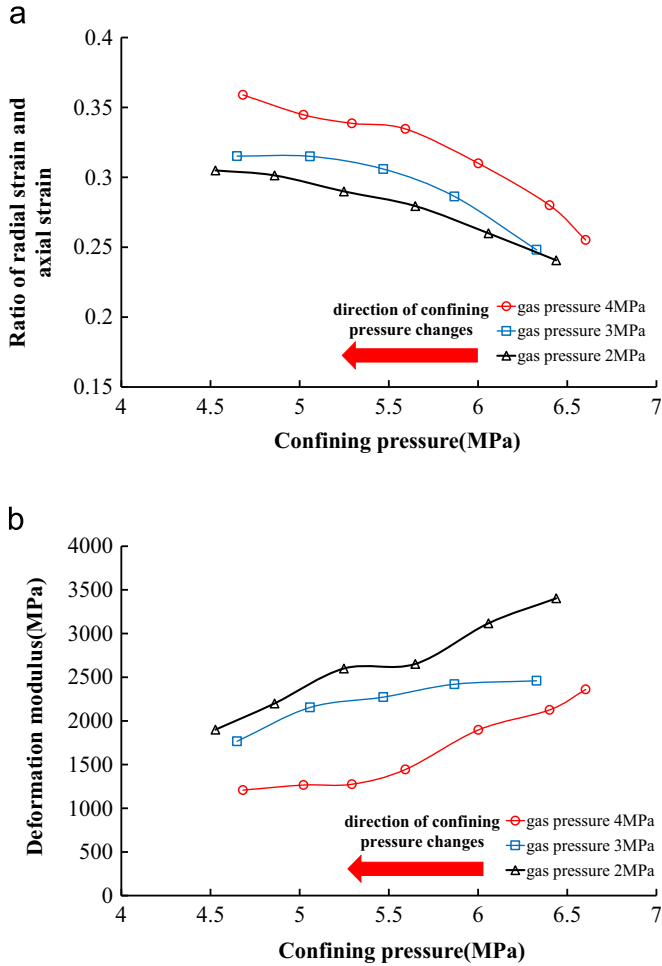


Fig. 13. Relationship between the deformation parameters and confining pressure. (a) Relationship between the ratio of radial strain to axial strain and confining pressure. (b) Relationship between the deformation modulus and confining pressure.

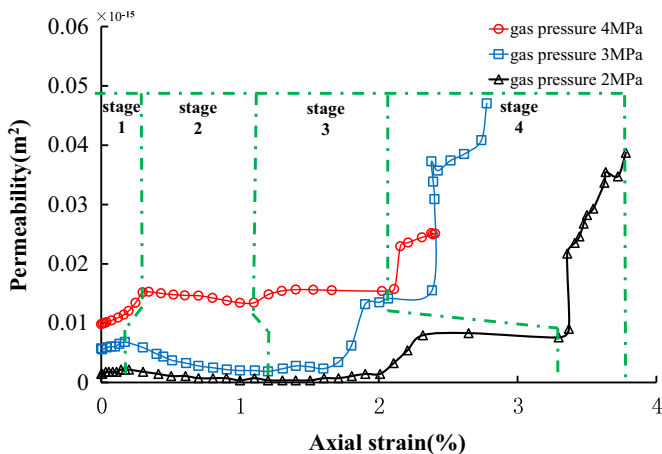


Fig. 14. Effect of gas pressure on the permeability-axial strain curves under the SUL path.

with gas pressure after the gas pressure exceeded some critical value, such as 2 MPa. The swelling rate of the coal matrix also became slower. From this point, the decrease of effective stress began to play the dominant role in the permeability evolution. The permeability of coal started to increase.

Fig. 15 compares the permeability-gas pressure curves under different stages of the SUL path. Fig. 15(a) shows the relationship

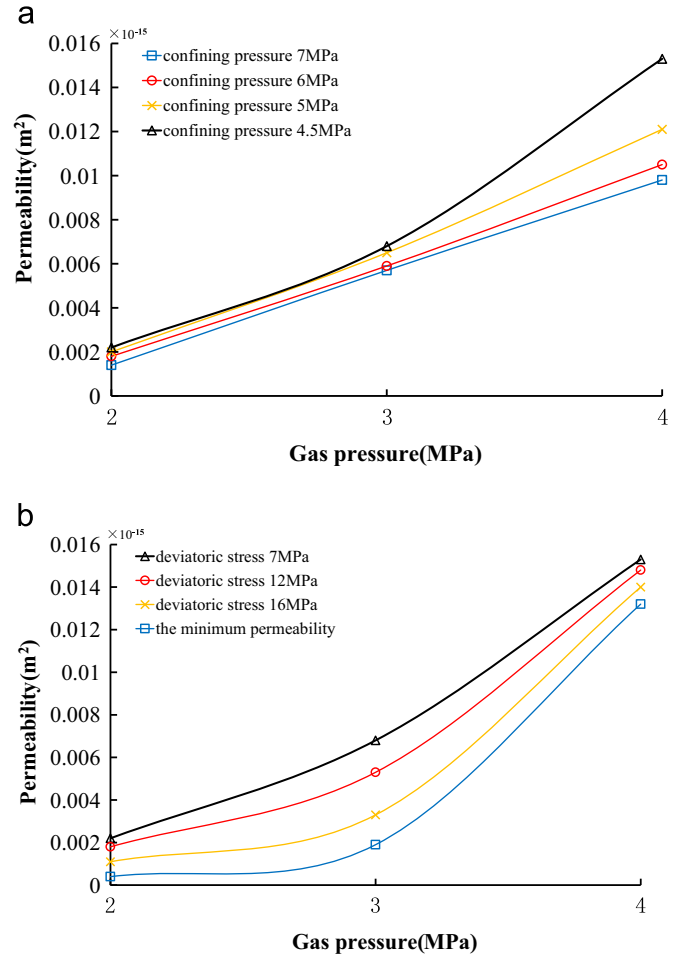


Fig. 15. Effect of stress on the permeability-gas pressure curves in the SUL tests. (a) In the process of the SUL. (b) In the process of only axial stress loading.

between the permeability and gas pressure in the process of SUL when the confining stress is 4.5, 5, 6, and 7 MPa. Fig. 15(b) presents the evolution of permeability with gas pressure when the deviatoric stress is at different levels. This deviatoric stress is achieved by loading the axial stress only after the confining stress reached 4.5 MPa. It is noted that the permeability in the hydrostatic pressure state was $0.0098 \times 10^{-15} \text{ m}^2$, $0.0057 \times 10^{-15} \text{ m}^2$ and $0.0014 \times 10^{-15} \text{ m}^2$ when the gas pressure was 4 MPa, 3 MPa, and 2 MPa, respectively. Obviously, the permeability decreased with decreasing gas pressure. The permeability of coal gradually increased to $0.0153 \times 10^{-15} \text{ m}^2$, $0.0068 \times 10^{-15} \text{ m}^2$ and $0.0022 \times 10^{-15} \text{ m}^2$, respectively, in the process of the SUL path. The permeability of coal decreased slowly in the stage of loading only axial stress. The minimum permeability was $0.0132 \times 10^{-15} \text{ m}^2$, $0.0019 \times 10^{-15} \text{ m}^2$ and $0.0004 \times 10^{-15} \text{ m}^2$ and was observed around the yield point.

5. Conclusion

The evolution of abutment stress was monitored at LW face 3211 of Songzao Mine in Chongqing, China, to obtain the mining-induced stress path in front of the working face. The concentration coefficient of the abutment stress was obtained, and the loading rate of the axial stress and the unloading rate of the confining stress were determined. Based on this stress path, a series of triaxial compression tests were conducted to measure the mining-induced mechanical behavior and gas permeability evolution of coal under triaxial loading and unloading conditions. The stress-strain-permeability relationships were closely observed in the

complete process from the elastic deformation to specimen failure. The effects of the gas pressure and deformation stages were explored, and the implication for coal mining operations were discussed. Based on these results, the following understandings and conclusions can be drawn:

First, the stress path in front of the working face was obtained by the field monitoring and measurement during the mining process of a protective layer. The monitoring results showed that the stress reached its peak at the point 18 m ahead of the LW face and then decreased. The concentration coefficient was approximately 1.5–2.0 for the abutment stress.

Second, the SUL path has significant impacts on both the peak strength and failure pattern. The peak deviatoric stress and the corresponding axial strain of coal under the SUL path were much lower than those under the CTC path. The ratio of radial strain to axial strain increased, and the deformation modulus decreased in the process of the SUL path.

Third, the permeability evolution of coal was different under the SUL and CTC paths. Under the SUL path, the permeability in the whole process can be divided into four stages: the increasing stage in the process of SUL, decreasing stage, slowly increasing stage beyond the yield point and sharply increasing stage after the peak stress. The radial strain is the key variable affecting the evolution of permeability in SUL tests. The unloading effect of confining stress on the permeability cannot be ignored.

Fourth, higher gas pressures made coal looser in our experiments. For higher gas pressures, the peak deviatoric stress and the corresponding axial strain were lower, Poisson's ratio of coal was higher, and the elastic modulus was lower. Further, the permeability of coal was higher for higher gas pressures in the complete deformation process. Two competitive factors, matrix swelling and effective confining stress, determined the mechanical behavior and permeability evolution. On one hand, the effective stress of coal decreased as the gas pressure increased. This reduction of effective stress expanded the flow channels of coal and increased the permeability of coal. On the other hand, more gas was adsorbed for a higher gas pressure and caused the coal matrix to swell more. The matrix swelling narrowed the flow channels and reduced the permeability of coal. The permeability evolution depended on the two competitive factors in the particular environment.

Finally, the influences of the SUL path on the mechanical behavior and permeability evolution of coal should be considered in underground mining activities to accurately predict engineering responses of coal under mining conditions and prevent coal mines from dynamic disasters. Particularly, the lower peak stresses and higher permeability of coal during the mining process should be considered in the safety prediction of coal mines.

Acknowledgments

This study was financially supported by National Basic Research Program of China (973 Program, 2011CB201203), National Natural Science Foundation of China (51434003, 51204217, 51374256), Chongqing Graduate Student Research Innovation Project (CYB14008), Scientific Research Foundation of State Key Lab. of Coal Mine Disaster Dynamics and Control (2011DA105287-MS201212) and Chongqing Research Program of Application Foundation and Advanced Technology (CSTC2015JCYJA90009).

References

- Xie HP, Zhou HW, Liu JF, et al. Mining-induced mechanical behaviors in coal seams under different mining layouts. *J China Coal Soc.* 2011;36:1067–1074.
- John GH, Hani SM. Numerical modelling of ore dilution in blasthole stoping. *Int J Rock Mech Min Sci.* 2007;44:692–703.
- Wang Z, Hu QT, Wen GC, Sun DL. Study on the distribution laws of mining pressure field and its control action on dynamic disasters in coal mines. *J China Coal Soc.* 2011;36:623–627.
- Guo H, Yuan L, Shen BT, Qu QD, Xue JH. Mining-induced strata stress changes, fractures and gas flow dynamics in multi-seam longwall mining. *Int J Rock Mech Min Sci.* 2012;54:129–139.
- Somerton WH, Söylemezoglu IM, Dudley RC. Effect of stress on permeability of coal. *Int J Rock Mech Min Sci.* 1975;12:129–145.
- Brace WF. A note on permeability changes in geologic material due to stress. *Pure Appl Geophys.* 1978;116:627–633 <http://dx.doi.org/10.1007/BF00876529>.
- Ghabezloo S, Sulem J, Guedon S, Martineau F. Effective stress law for the permeability of a limestone. *Int J Rock Mech Min Sci.* 2009;46:297–306 <http://dx.doi.org/10.1016/j.ijrmms.2008.05.006>.
- Enever JRE, Henning A. The relationship between permeability and effective stress for Australian coal and its implications with respect to coal-bed methane exploration and reservoir modeling. In: *Proceedings of the 1997 International Coal-bed Methane Symposium.*
- Vishal V, Ranjith PG, Pradhan SP, Singh TN. Permeability of sub-critical carbon dioxide in naturally fractured Indian bituminous coal at a range of down-hole stress conditions. *Eng Geol.* 2013;167:148–156.
- George SJD, Barakat MA. The change in effective stress associated with shrinkage from gas desorption in coal. *Int J Coal Geol.* 2001;45:105–113 [http://dx.doi.org/10.1016/S0166-5162\(00\)00026-4](http://dx.doi.org/10.1016/S0166-5162(00)00026-4).
- Chen ZW, Pan ZJ, Liu JS. Effect of the effective stress coefficient and sorption-induced strain on the evolution of coal permeability: Experimental observations. *Int J Greenh Gas Control.* 2011;5:1284–1293 <http://dx.doi.org/10.1016/j.ijggc.2011.07.005>.
- Meng ZP, Li GQ. Experimental research on permeability of high-rank coal under a varying stress and its influencing factors. *Eng Geol.* 2013;162:108–117 <http://dx.doi.org/10.1016/j.enggeo.2013.04.013>.
- Vishal V, Ranjith PG, Singh TN. An experimental investigation on behaviour of coal under fluid saturation, using acoustic emission. *J Nat Gas Sci Eng.* 2015;22:428–436 <http://dx.doi.org/10.1016/j.jngse.2014.12.020>.
- Vishal V, Singh TN, Ranjith PG. Influence of sorption time in CO₂-ECBM process in Indian coals using coupled numerical simulation. *Fuel.* 2015;139:51–58 <http://dx.doi.org/10.1016/j.fuel.2014.08.009>.
- Chen HD, Cheng YP, Zhou HX, Li W. Damage and permeability development in coal during unloading. *Rock Mech Rock Eng.* 2013;46:1377–1390 <http://dx.doi.org/10.1007/s00603-013-0370-2>.
- Cai YD, Liu DM, Jonathan PM, Pan ZJ, Elsworth D, Yao YB, Li JQ, Guo XQ. Permeability evolution in fractured coal-combining triaxial confinement with X-ray computed tomography, acoustic emission and ultrasonic techniques. *Int J Coal Geol.* 2014;122:91–104 <http://dx.doi.org/10.1016/j.coal.2013.12.012>.
- Zhang J, Standifird WB, Roegiers JC, Zhang Y. Stress-dependent fluid flow and permeability in fractured media: from lab experiments to engineering applications. *Rock Mech Rock Eng.* 2007;40:3–21 <http://dx.doi.org/10.1007/s00603-006-0103-x>.
- Qiu SL, Feng XT, Xiao JQ, Zhang CQ. An experimental study on the pre-peak unloading damage evolution of marble. *Rock Mech Rock Eng.* 2014;47:401–419 <http://dx.doi.org/10.1007/s00603-013-0394-7>.
- Wang SG, Elsworth D, Liu JS. Mechanical behaviors of methane infiltrated coal: the roles of gas desorption, stress level and loading rate. *Rock Mech Rock Eng.* 2013;46:1377–1390 <http://dx.doi.org/10.1007/s00603-012-0324-0>.
- Wang SG, Elsworth D, Liu JS. Permeability evolution during progressive deformation of intact coal and implications for instability in underground coal seams. *Int J Rock Mech Min Sci.* 2013;58:34–45 <http://dx.doi.org/10.1016/j.ijrmms.2012.09.005>.
- Zhao YS, Hu YQ, Yang D, Wei JP. The experimental study on the gas seepage law of rock-related to adsorption under 3D stresses. *Chin J Rock Mech Eng.* 1999;18:651–653 <http://dx.doi.org/10.3321/j.issn:1000-6915.1999.06.007>.
- Tang JP, Pan YS, Li CQ, Shi Q, Dong ZX. Experimental study on effect of effective stress on adsorption and seepage of coal-bed methane. *Chin J Rock Mech Eng.* 2006;25:1563–1568 <http://dx.doi.org/10.3321/j.issn:1000-6915.2006.08.007>.
- Pan ZJ, Connell LD, Camilleri M. Laboratory characterisation of coal reservoir permeability for primary and enhanced coalbed methane recovery. *Int J Coal Geol.* 2010;82:252–261 <http://dx.doi.org/10.1016/j.coal.2009.10.019>.
- Li JQ, Liu DM, Yao YB, Cai YD, Chen Y. Evaluation and modeling of gas permeability changes in anthracite coals. *Fuel.* 2013;111:606–612 <http://dx.doi.org/10.1016/j.fuel.2013.03.063>.
- Vishal V, Ranjith PG, Singh TN. CO₂ permeability of Indian bituminous coals: Implications for carbon sequestration. *Int J Coal Geol.* 2013;105:36–47 <http://dx.doi.org/10.1016/j.coal.2012.11.003>.
- Vishal V, Singh TN. A laboratory investigation of permeability of coal to supercritical CO₂. *Geotech Geol Eng.* 2015;33:1009–1016 <http://dx.doi.org/10.1007/s10706-015-9882-8>.
- Chareonsuppanimit P, Mohammad SA, Robinson RL, Gasem KAM. Modeling gas-adsorption-induced swelling and permeability changes in coals. *Int J Coal Geol.* 2014;121:98–109 <http://dx.doi.org/10.1016/j.coal.2013.11.009>.
- Zhou SN, Lin BQ. *The Theory of Gas Flow and Storage in Coal Seams.* Beijing: China Coal Industry: Publishing House; 1996.
- Wang L, Cheng YP, Li FR, Wang HF, Liu HB. Fracture evolution and pressure relief gas drainage from distant protected coal seams under an extremely thick key stratum. *J China Univ Min Technol.* 2008;18:182–186 [http://dx.doi.org/10.1016/S1006-1266\(08\)60039-5](http://dx.doi.org/10.1016/S1006-1266(08)60039-5).
- Yin GZ, Jiang CB, Wang JG, Xu J. Combined effect of stress, pore pressure and temperature on methane permeability in anthracite coal: An experimental study. *Transp Porous Media.* 2013;100:1–16 <http://dx.doi.org/10.1007/s11242-013-0202-6>.
- Hildenbrand A, Schlömer S, Krooss BM. Gas breakthrough experiments on fine-grained sedimentary rocks. *Geofluids.* 2002;2:3–23 <http://dx.doi.org/10.1046/j.1468-8123.2002.00031.x>.